Droplet coalescence by molecular dynamics and phase-field modeling

View Online   Export Citation   CrossMark

Matthias Heinen,[1] (iD) Marco Hoffmann,[2] (iD) Felix Diewald,[3] Steffen Seckler,[4] Kai Langenbach,[5] and Jadran Vrabec[1,a)] (iD)

AFFILIATIONS

[1]Thermodynamics and Process Engineering, Technical University of Berlin, 10587 Berlin, Germany
[2]Institute of Applied Mechanics, Technical University of Kaiserslautern, 67653 Kaiserslautern, Germany
[3]Department of Optimization, Fraunhofer ITWM, 67663 Kaiserslautern, Germany
[4]Scientific Computing in Computer Science, Technical University of Munich, 85748 Garching, Germany
[5]Thermal Process Engineering, Innsbruck University, 6020 Innsbruck, Austria

[a)]Author to whom correspondence should be addressed: vrabec@tu-berlin.de

ABSTRACT

Coalescence of argon droplets with a radius of 25, 50, and 100 nm is studied with computational methods. Molecular dynamics (MD) simulations are carried out to generate reference data. Moreover, a phase-field model resting on a Helmholtz energy equation of state is devised and evaluated by computational fluid dynamics (CFD) simulations. Exactly the same scenarios in terms of geometry, fluid, and state are considered with these approaches. The MD and CFD simulation results show an excellent agreement over the entire coalescence process, including the decay of the inertia-induced oscillation of the merged droplet. Theoretical knowledge about the asymptotic behavior of coalescence process regimes is confirmed. All considered scenarios cross from the inertially limited viscous regime over to the inertial regime because of the low shear viscosity of argon. The particularly rapid dynamics during the initial stages of the coalescence process in the thermal regime is also captured by the phase-field model, where a closer look at the liquid density reveals that metastable states associated with negative pressure are attained in the emerging liquid bridge between the coalescing droplets. This demonstrates that this model is even capable of adequately handling the onset of coalescence. To speed up CFD simulations, the phase-field model is transferred to coarser grids through an interface widening approach that retains the thermodynamic properties including the surface tension.

Published under an exclusive license by AIP Publishing. https://doi.org/10.1063/5.0086131

I. INTRODUCTION

Droplet coalescence is ubiquitous in nature, e.g., during the formation of raindrops, and in technical applications, like viscous sintering[1] or spray cooling.[2] Recently, Jin *et al.*[3] presented a general overview, discussing ways to externally induce coalescence, which is a key factor for designing lab-on-a-chip devices. Hence, there is an ongoing effort to expand its understanding and to develop numerical models for the design and optimization of applications. Therefore, coalescence has been investigated by numerous theoretical,[4–9] experimental,[10–24] and numerical[8,9,21–36] approaches, and also review articles[37,38] have appeared.

The coalescence process between two droplets is characterized by the formation of a bridge at their initial contact point that develops into a meniscus at its outer boundary. According to the Young–Laplace law, a strong pressure gradient emerges at this meniscus due to an initially strong negative curvature so that liquid flows

in-between the droplets driven by the surface tension γ, causing the bridge to grow. The growth rate of the bridge also depends on the velocity with which the liquid can flow from the droplet interior into the bridge. For the asymptotic limit of Stokes flow, Hopper[4] provided an analytical solution for the two-dimensional case of viscous cylinders. Later, Eggers *et al.*[5] showed the applicability of Hopper's solution to the case of spherical droplets. However, they remarked that the Stokes approximation is only valid up to a Reynolds number Re ~ 1 so that for low shear viscosity η, the flow is expected to become dominated by inertial rather than viscous forces, once the transition regime has been passed. The scaling laws derived from this analysis describe some aspects of droplet coalescence dynamics. The process begins in a viscous regime, where the time evolution of the bridge radius r_b in terms of the initial droplet radius R approximately satisfies $r_b/R \sim -\tau/\tau_v \ln(\tau/\tau_v)$ for $r_b/R < 0.03$ with the time scale $\tau_v = \eta R/\gamma$.

In the case of sufficiently low shear viscosity, the flow characteristics will transition to an inertial (or inviscid) regime at later stages, where $r_b/R \sim (\tau/\tau_i)^{1/2}$ applies with the time scale $\tau_i = (\rho R^3/\gamma)^{1/2}$. Here, $\tau = t - t_0$ measures the time elapsed since the droplet contact at t_0, and ρ is the mass density.

While the 1/2 power law was confirmed by many experimental[13–17] and numerical[9,29–32] approaches, inconsistencies were revealed with respect to viscous scaling. Among others, Aarts et al.[14] found their experimental data to obey linear scaling $r_b/R \sim \tau/\tau_v$. Also, Paulsen et al.[19]—who employed an electrical method to probe the very early stages of droplet coalescence (down to 10 ns after contact) in the laboratory—could not corroborate the logarithmic correction[5] and attributed the discrepancy to an inappropriate length scale of the Reynolds number. They suggested the bridge height r_b^2/R instead of the bridge radius r_b as the dominant length scale. Using this alternative length scale definition, they managed to collapse their experimental data covering a variation of shear viscosity over two orders of magnitude onto a single curve, pointing to the universality of that scaling law. For this purpose, the data were rescaled by the crossover time τ_c and crossover radius r_c obtained from the condition $\mathrm{Re} = 1$. Subsequently, Paulsen et al.[22] identified the inertially limited viscous (ILV) regime, upstream of the Stokes regime. They argued that the latter can only be attained once the inward force of the bridge generated by the surface tension is sufficiently large to induce an asymptotic acceleration of the coalescing droplet's centers of mass. Consequently, this condition leads to a threshold criterion for entering the Stokes regime. Paulsen et al.[22] presented this in the form of a revised phase diagram for coalescence, by plotting the Ohnesorge number $\mathrm{Oh} = \eta/\sqrt{\rho\gamma R}$ over the reduced bridge radius r_b/R. This phase diagram indicates that coalescence always begins in the ILV regime. Depending on Oh, there is a subsequent crossover to either the Stokes regime (Oh > 1) or the inertial regime (Oh < 1).

Reviewing the development of theory on coalescence dynamics, it is noticeable that it has benefited greatly from numerical investigations. For instance, Paulsen et al.[22] were able to corroborate their discovery of the ILV regime by streamline analyses from computational fluid dynamics (CFD) simulations, showing qualitatively different flow patterns for all three regimes identified at that time (ILV, Stokes, and inertial). Recently, Perumanath et al.[39] showed with molecular dynamics (MD) simulation that another so-called thermal regime upstream of the classical hydrodynamic regimes exists, where the bridge growth dynamics is dominated by "collective molecular jumps." MD simulation is particularly suited for this regime, since the length and time scales that this method can resolve are on the order of picometers and picoseconds. Coalescence processes with their rapid dynamics, especially at the very beginning, can thus be studied with atomistic detail, cf. Fig. 1 (Multimedia view). Another advantage is that the interface and its properties, such as surface tension, evolve naturally during MD simulation, without interventions or assumptions about its nature. Residing on a lower level of abstraction, the sole input for MD simulations is the molecular interaction model. It entails, however, a large computational effort; therefore, such studies[32,39–43] have been limited to nanoscopic droplets so far.

To extend the accessible length and time scales to those of hydrodynamics, Hoogerbrugge and Koelman[45] devised the dissipative particle dynamics (DPD) simulation technique. Compared with MD, the computational effort is reduced by combining several molecules into
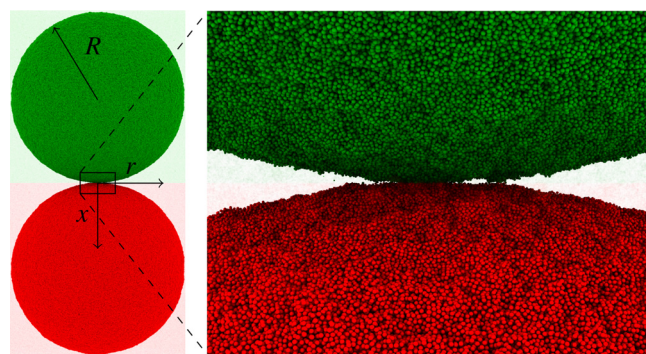

FIG. 1. Snapshot of the initial configuration of the $R = 100$ nm scenario consisting of about 200×10^6 molecules, rendered by the open source visualization framework *MegaMol*.[44] Molecules constituting the two droplets were colored green and red, respectively, to follow their propagation. In order to obtain a clear view on the interface, molecules of the vapor phase were rendered with low opacity. The magnified view on the contact region illustrates the small initial distance of a single molecule diameter. For the droplets with $R = 25$ nm, the coalescence process was rendered as a sequence. Multimedia view: https://doi.org/10.1063/5.0086131.1

coarse-grained DPD particles. The challenge is then to appropriately calibrate their interaction potential, e.g., to experimental data or MD simulation results. Recently, a first work[46] appeared corroborating the universality of coalescence scaling laws by means of DPD simulations.

With traditional CFD methods, the Navier–Stokes (NS) equations are solved directly,[21,24–26] which was done for coalescing liquid–liquid systems[25,26] and liquid droplets surrounded by a gas phase.[21,24,33] Next to classical CFD simulations, several publications[27–29] used the lattice Boltzmann (LB) method to study coalescence. In both NS- and LB-based simulations, the interface requires specific treatment due to its small width and surface tension, which is commonly not directly included in the pressure tensor. Generally, there are two ways to model the interface. A sharp interface defines a discontinuity of the thermodynamic properties, while a diffuse interface imposes a continuous transition over a finite width. The first additionally requires an interface[24,25] or boundary tracking method[21] to apply the surface tension. The phase-field method,[47–50] which is a diffuse interface method, is based on the ideas of Cahn and Hillard,[51] who proposed a free energy functional that depends on a scalar state variable and its spatial derivative. This scalar property, referred to as order parameter in phase-field models, can be, e.g., the mole fraction[25–27] for binary liquid systems or the density[29] for vapor–liquid systems.

The CFD method presented in this work is based on a phase-field model and the thermodynamic properties of the fluid are described by a Helmholtz energy functional that consists of a density and a density gradient-dependent part. There are physically sound expressions for the Helmholtz energy, i.e., equations of state (EoS), like the perturbed chain statistical associating fluid theory (PC-SAFT),[52] perturbed truncated and shifted (PeTS),[53] or the co-oriented fluid functional equation for electrostatic interactions (COFFEE),[54] to properly describe pure fluids and mixtures. Combined with classical density gradient theory,[51,55,56] the gradient term of phase-field models can be understood as a resistance to the formation of an interface and is related to the second moment of the direct correlation function.[57] Using the PeTS EoS,[53] some of the present authors have shown that vapor–liquid interfaces of pure fluids[58] and mixtures[59] in static[58,59] or

dynamic[60] scenarios with[60] and without[58,59] the presence of solid walls can be described almost solely based on this Helmholtz energy EoS. The only adjustable parameter of the density gradient term was shown to be state-independent.[53] For dynamic scenarios, additional models for the transport properties are necessary.[61] Such phase-field models have the advantage that all thermodynamic properties are inherently included. However, the length and time scales that need to be considered become small, demanding for a fine discretization in space and time, if no additional measures are taken. The present phase-field model does not require any *a priori* assumptions about the fluid, its phase equilibrium, or the investigated process. The only requirements are a Helmholtz energy EoS that appropriately covers the metastable and unstable regions by having a single van der Waals loop, as well as expressions for the shear viscosity and the surface tension.

In a concerted effort, the phase-field model and MD simulation were applied in this work to coalescence, considering argon droplets in three sizes with an initial radius ranging from 25 to 100 nm surrounded by coexisting vapor.

II. MOLECULAR DYNAMICS

Resting on statistical mechanics, MD simulation is a physically sound approach to study phenomena like droplet coalescence with an atomistic level of detail. Except for the force field describing the intermolecular interactions, practically no further assumptions have to be made. Consequently, the results from this approach are well suited to serve as a benchmark to evaluate macroscopic solutions that involve much more severe assumptions. This opportunity was exploited here to assess the phase-field model described in Sec. III and findings from the literature. Since the applicability of continuum assumptions reaches its limit on the nanoscale, comparatively large droplets were prepared to allow for a direct comparison, considering exactly the same scenario in terms of geometry, fluid, and state.

The truncated and shifted Lennard-Jones (LJTS) potential was chosen for the intermolecular interactions. Since it has a small cutoff radius of 2.5 molecule diameters σ and no long range corrections have to be taken into account, it is computationally rather cheap. Moreover, the PeTS EoS[53] is available for the fluid defined by this potential that is suitable for phase-field modeling. The LJTS potential can be parameterized to adequately represent the thermophysical properties of the noble gases and methane.[62] In fact, the energy parameter $\epsilon/k_B = 137.9$ K, the size parameter $\sigma = 3.3916$ Å, and the molar mass $M = 39.948$ g mol^{-1} were specified such that the present simulations mimic argon.[62]

Three droplet sizes were considered, having an initial radius of $R = 25$, 50, and 100 nm. To create an initial configuration of the coalescence process, the droplets were first prepared in a vapor–liquid equilibrium simulation at the desired temperature $T = 110$ K, which corresponds to $\approx 73\%$ of the critical temperature. The resulting saturated liquid and vapor densities that slightly depend on the droplet size were in good agreement with a correlation for exactly that inhomogeneous fluid.[62] Subsequently, two copies of equilibrated droplets were arranged along the x axis of a cuboid volume with a distance of a single molecule diameter, surrounded by vapor in equilibrium with the liquid, cf. Fig. 1. In total, the generated systems consisted of about 3, 25, and 200×10^6 molecules. All MD simulations were conducted with the open source code *ls1 mardyn*[63] that is well suited for massively parallel execution.[64]

To capture the rapid dynamics of the coalescence process, the spatially and temporally resolved density distribution was sampled during simulation. For this purpose, the computational domain was divided into equidistant cylinder shells around the x axis, exploiting the system's rotational symmetry, and equidistant slices along the x axis, both with a width of $\sim 3\sigma/4$. Within these sampling bins in the form of cylinder shell elements, the mass density

$$\rho = \frac{M}{N_A} \frac{\langle N \rangle}{V(r)} \qquad (1)$$

was averaged over a period of 5000 MD integration time steps with $\Delta t = 2$ fs, thus amounting to 10 ps. $V(r)$ is the bin volume and depends on the shell radius r, i.e., distance to the x axis; $\langle N \rangle$ is the average number of molecules counted within the according bin; and N_A is the Avogadro constant. Because of the largely varying cylinder shell volumes, the statistical quality of the data sampled near the x axis is lower than elsewhere.

The computational effort of the conducted MD simulations is summarized in Table I.

III. PHASE-FIELD MODEL

To investigate droplet coalescence, the NS equations were solved on the basis of a phase-field model. The mass and momentum balances in the computational domain $\mathscr{B}$ are

$$\dot{\rho} + \rho \nabla \cdot \mathbf{v} = 0, \qquad (2)$$

$$\rho \dot{\mathbf{v}} = \nabla \cdot \boldsymbol{\sigma}. \qquad (3)$$

Here, $\rho(\mathbf{x}, t)$ and $\mathbf{v}(\mathbf{x}, t)$ denote the density and velocity as a function of position $\mathbf{x}$ and time t, the material time derivative is $(\dot{\cdot}) = \mathrm{d}(\cdot)/\mathrm{d}t$ and the symbol ∇ stands for the nabla operator. The temperature in the domain was held constant, and bulk viscous effects and volume forces, like gravity, were neglected. The Cauchy stress tensor $\boldsymbol{\sigma}$ is given by

$$\boldsymbol{\sigma} = 2\eta \left[\nabla^s \mathbf{v} - \frac{1}{3} \mathrm{tr}(\nabla^s \mathbf{v}) \mathbf{1} \right] + [f - \rho\mu] \mathbf{1} - \kappa \nabla\rho \otimes \nabla\rho, \qquad (4)$$

with $\nabla^s(\cdot) = (\nabla(\cdot) + (\nabla(\cdot))^{\mathrm{T}})/2$, trace $\mathrm{tr}(\cdot)$, identity matrix $\mathbf{1}$, dyadic product $\otimes$, chemical potential μ, and influence parameter κ that was adjusted to the surface tension.[53] This constitutive relation includes a viscous part as well as pressure and surface tension resulting from the phase-field model. The Helmholtz energy density f reads

$$f(\rho, \nabla\rho) = \rho a + \kappa \frac{1}{2} |\nabla\rho|^2, \qquad (5)$$

TABLE I. Computational effort for the MD simulations in terms of core-h spent on the national supercomputer HPE Apollo (Hawk) at the High Performance Computing Center Stuttgart (HLRS), depending on the initial droplet radius R, volume of the computational domain V (width × height × depth), number of molecules, number of time steps N_{ts}, and the resulting physical time period t.

R (nm)	V (nm^3)	N (–)	N_{ts} (–)	t (ns)	core-h (h)
25	150 × 100 × 100	3.2×10^6	5.0×10^6	10.0	1.9×10^5
50	300 × 200 × 200	2.5×10^7	17.2×10^6	34.3	2.7×10^6
100	600 × 400 × 400	2.0×10^8	10.2×10^6	20.3	8.8×10^6

where the Helmholtz energy a was specified by the PeTS EoS,[53] which adequately covers metastable and unstable states and appropriately describes the transition between the coexisting bulk phases. An expression for the shear viscosity η that is based on MD simulation data[61] was taken from Ref. 60.

In conjunction with the NS equations, the chemical potential, given by

$$\mu = \frac{\partial f(\rho, \nabla \rho)}{\partial \rho} - \nabla \cdot \frac{\partial f(\rho, \nabla \rho)}{\partial \nabla \rho}, \quad (6)$$

was treated as a variable and solved at every time step.

Unlike MD, CFD simulations can be applied to problems exceeding the nanoscale because the computational effort is substantially lower. This is evident from the core-h spent on the supercomputers, which is three orders of magnitude larger for MD simulations, cf. Tables I and II. For the finite element (FE) implementation, the interface width nonetheless represents a limiting factor for the mesh size because it has to be resolved by at least four grid elements to ensure a stable computation. To overcome this scale limitation, the interface was artificially widened following Ref. 65.

For this purpose, a scaled formulation of the Helmholtz energy density f_{sc} was introduced as follows:

$$f_{sc}(\rho, \nabla \rho) = \alpha \underbrace{(\rho a(\rho) - \mu^s \rho + p^s)}_{\omega(\rho)} + \mu^s \rho - p^s + \beta \frac{1}{2} |\nabla \rho|^2. \quad (7)$$

Here, p^s denotes the vapor pressure and μ^s the chemical potential at saturation. The two constants α and β scale the grand potential density $\omega(\rho)$ and the density gradient-dependent part of the Helmholtz energy density, respectively. They are defined by the specified interface width L_{sc}. When scaling the Helmholtz energy density, the thermodynamic properties of the system, except for the interface width, must not change. The first derivative of the scaled Helmholtz energy with respect to the density under saturation conditions reads

TABLE II. Computational effort for the CFD simulations in terms of core-h spent on the cluster *Elwetritsch* at Regionales Hochschulrechenzentrum Kaiserslautern (RHRK), depending on the initial droplet radius R, interface widening factor ξ, number of Q2P1 elements N_{el} used for the discretization of the computational domain, time step width Δt, number of time steps N_{ts}, and the resulting physical time period t. The entry of core-h for $R = 100$ nm, $\xi = 4$ was omitted because that measurement failed.

R (nm)	ξ (–)	N_{el} (–)	Δt (ps)	N_{ts} (–)	t (ns)	core-h (h)
25	1	336×144	1	400	0.4	9.7
25	2	168×72	1	400	0.4	4.2
25	4	84×36	1	400	0.4	2.4
25	1	336×144	10	1040	10.4	33.1
50	1	672×288	1	400	0.4	38.0
50	2	336×144	1	400	0.4	9.6
50	4	168×72	1	400	0.4	4.1
50	1	672×288	20	1270	25.4	398.5
100	1	1344×576	1	400	0.4	149.7
100	2	672×288	1	400	0.4	37.7
100	4	336×144	1	400	0.4	9.1
100	4	336×144	40	2040	81.6	$\cdots$

$$\left. \frac{\partial(f_{sc}(\rho, \nabla \rho))}{\partial \rho} \right|_{\rho \in \{\rho', \rho''\}} = \alpha \underbrace{\left(\left. \frac{\partial(\rho a(\rho))}{\partial \rho} \right|_{\rho \in \{\rho', \rho''\}} - \mu^s \right)}_{=0} + \mu^s. \quad (8)$$

This is identical with the original Helmholtz energy formulation (6) and retains the consistency of the saturated densities. Furthermore, the second derivative of the scaled Helmholtz energy with respect to the density, given by

$$\frac{\partial^2(f_{sc}(\rho, \nabla \rho))}{\partial \rho^2} = \alpha \frac{\partial^2(\rho a(\rho))}{\partial \rho^2}, \quad (9)$$

is equal to the second derivative of the original Helmholtz energy formulation, except for the constant α. Consequently, the spinodals, where the second derivative of the Helmholtz energy density with respect to the density is zero, remain unaltered. The effects of scaling on the Helmholtz energy and grand potential density are visualized in Fig. 2. For $\alpha = 1$, the curves are identical with the original Helmholtz
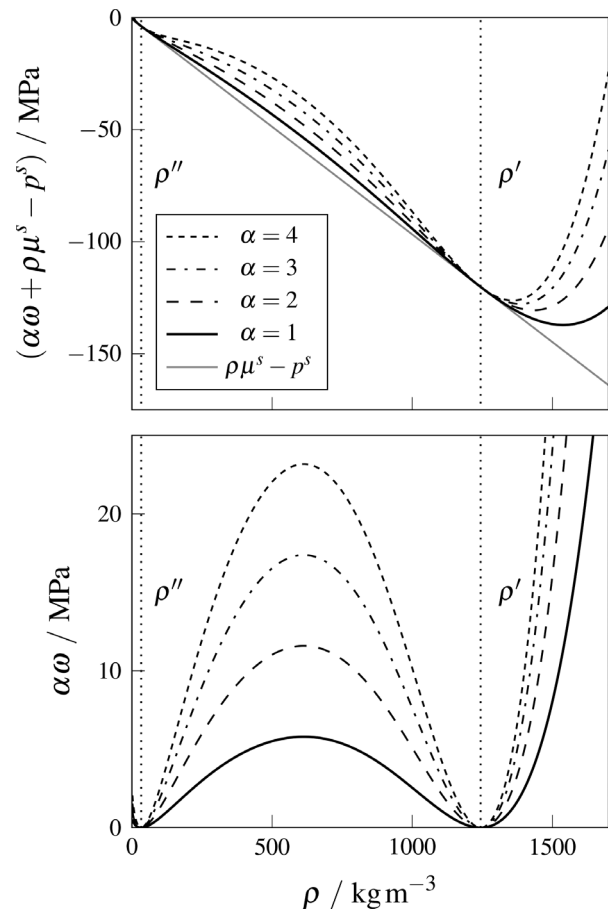

FIG. 2. Scaled Helmholtz energy density (top) and grand potential density (bottom) over mass density ρ at a temperature of $T = 110$ K for different values of α. The two minima of the grand potential density are located at the saturated densities ρ' and ρ''.

energy formulation. Consistent saturated densities and an unaltered unstable region width are retained for varying values of α.

The scaling of the interface width was carried out under the assumption of a planar interface. However, nanoscopic droplets have slightly deviating interface properties due to their strong curvature and also the coexisting densities do not exactly correspond to those of a planar interface.[62] Since the purpose of interface widening is to deal with larger scenarios, these differences were neglected. The scaled width L_{sc} of a planar interface that is perpendicular to the x axis was defined as

$$\left.\frac{d\rho}{dx}\right|_{x=x_i} = \frac{\rho' - \rho''}{L_{sc}} \quad \text{with} \quad x_i = x(\rho_{xi} = (\rho' + \rho'')/2), \quad (10)$$

with x_i being the position where the density takes the average of the saturated liquid and vapor densities ρ' and ρ''. With this definition, a tangent is laid out on the density profile at x_i. The interface width is then the distance of this tangent along the x axis between its two intersection points with the saturated densities ρ' and ρ'', respectively.

In addition, the surface tension taken from Ref. 62 had to be retained. The necessary requirement is

$$\gamma = \frac{\Omega}{A}, \quad (11)$$

where A is the interface area and Ω the grand potential. For a planar interface under equilibrium that is perpendicular to the x axis,

$$\Omega = A \int_{-\infty}^{+\infty} \left[\alpha\omega(\rho) + \frac{1}{2}\beta|\nabla\rho|^2 \right] dx. \quad (12)$$

Following the approach presented in Ref. 51 yields

$$\alpha\omega(\rho) = \frac{1}{2}\beta|\nabla\rho|^2. \quad (13)$$

This allows to rewrite the integral over x in Eq. (12) into an integral over ρ using

$$dx = \sqrt{\frac{\beta}{2\alpha\omega(\rho)}}d\rho, \quad (14)$$

leading to

$$\int_{\rho''}^{\rho'} \sqrt{2\alpha\beta\omega(\rho)}d\rho = \gamma. \quad (15)$$

With Eq. (14), the definition of the interface width L_{sc} can be rewritten as

$$\left.\frac{d\rho}{dx}\right|_{x=x_i} = \frac{\rho' - \rho''}{L_{sc}} = \sqrt{\frac{2\alpha\omega(\rho = \rho_{xi})}{\beta}}. \quad (16)$$

Solving Eqs. (15) and (16) yields

$$\alpha = \frac{\rho' - \rho''}{2\sqrt{\omega(\rho = \rho_{xi})}\int_{\rho''}^{\rho'}\sqrt{\omega(\rho)}\,d\rho}\frac{\gamma}{L_{sc}}, \quad (17)$$

$$\beta = \frac{\sqrt{\omega(\rho = \rho_{xi})}}{(\rho' - \rho'')\int_{\rho''}^{\rho'}\sqrt{\omega(\rho)}\,d\rho}\gamma L_{sc}. \quad (18)$$

The interface width can be widened by specifying a value for L_{sc}, which allows to reduce the number of elements needed to discretize the computational domain. Instead, or even additionally, an adaptive grid could have been used to resolve the interface and reduce the number of elements even further, but this was beyond the scope of this work.

The computational domain was formed utilizing a cylindrical coordinate system with a radial distance r, angle φ, and length x. Due to the radial symmetry of the investigated coalescence scenario, all vectorial quantities in the direction of φ and all derivatives with respect to the angle φ vanish, i.e.,

$$v_\varphi = 0, \quad \frac{\partial \mathbf{v}}{\partial\varphi} = 0, \quad \frac{\partial\mu}{\partial\varphi} = 0, \quad \frac{\partial\rho}{\partial\varphi} = 0; \quad (19)$$

thus, two-dimensional discretization suffices. The boundary conditions for the computational domain $\mathcal{B}$ read

$$\mathbf{v} = 0 \quad \text{on} \quad \partial\mathcal{B}\backslash\partial\mathcal{B}_{r=0}, \quad (20)$$

$$v_r = 0 \quad \text{on} \quad \partial\mathcal{B}_{r=0}, \quad (21)$$

$$\nabla\rho \cdot \boldsymbol{n} = 0 \quad \text{on} \quad \partial\mathcal{B}. \quad (22)$$

Here, v_r denotes the velocity perpendicular to the symmetry axis $\partial\mathcal{B}_{r=0}$ and $\boldsymbol{n}$ the outer normal to the boundary of the computational domain $\partial\mathcal{B}$, cf. Fig. 3. Due to these boundary conditions, the mass in the computational domain remains constant. The temperature was throughout specified to be constant at $T = 110\,\text{K}$. The setup was initialized by a radial density profile approximated by
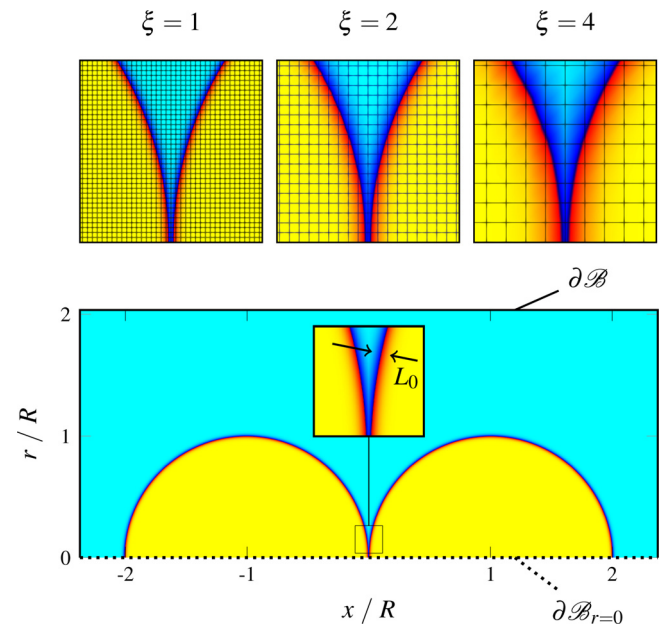

FIG. 3. Bottom: setup of the computational domain for the coalescence scenario. The magnified view on the droplets' contact region emphasizes the initial interface width $L_0 = L$, where L is the interface width that was found under equilibrium conditions. Top: detailed views with grids indicating the discretization used for the FE scheme. In simulations with a widened interface $L_{sc} = \xi L$, for $\xi = 2$, half as many but twice as large grid elements were used compared to the simulations without employing the interface widening approach ($\xi = 1$).

$$\rho(r) = \frac{\rho' - \rho''}{2}\left[\tanh\left(\frac{2(R-r)}{L_0}\right) + 1\right] + \rho'', \quad (23)$$

where the saturated liquid and vapor densities ρ' and ρ'' were taken from Ref. 62. Following Ref. 58, a value of $L_0 \approx 2.5\sigma$ was used for the initial interface width. In simulations employing the interface widening approach, a scaled interface width $L_{sc} = \xi L$ set to a multiple of the true interface width L under equilibrium conditions was used instead. In the present work, simulations with $\xi = 1$, 2, and 4 were performed.

An FE implementation was used as a numerical solution scheme; details are provided in Ref. 65. For the coalescence scenario considering two droplets with an initial radius of $R = 25$ nm, a rectangle of 336×144 Q2P1 elements was used to discretize a domain of about 120×50 nm². The larger scenarios were scaled proportionally in terms of the domain's extent and element count. Consequently, these were doubled twice for $R = 50$ nm and $R = 100$ nm. For simulations employing the interface widening approach, however, the number of elements was scaled down by the factor ξ in both dimensions, cf. Fig. 3, yielding four ($\xi = 2$) and 16 times ($\xi = 4$) fewer elements and, thus, reduced the computational effort roughly by a factor ξ^2, as summarized in Table II. It should be noted, however, that the computational effort for different time increments varied significantly, depending on the convergence of the Newton method. As in the MD simulations, the initial distance between the two droplets was a single molecule diameter σ. At $t = 0$, the velocity $\mathbf{v} = 0$ was set in the entire domain. Figure 3 depicts the initialized domain for the $R = 25$ nm scenario. The time discretization was chosen such that the numerical solution efficiency was optimal, while ensuring convergence of the Newton method. Because of the rapidly growing bridge in the early stages, a time step of $\Delta t = 1$ ps was used up to time $t = 400$ ps. For the later

stages, time steps of $\Delta t = 10$, 20, and 40 ps were used for the scenarios with $R = 25$, 50, and 100 nm, respectively.

IV. RESULTS

For a qualitative comparison of the simulation results, it is useful to superimpose the evolution of the coalescing droplets' interface contour obtained from MD and CFD simulations. Naively comparing states with equal elapsed time τ has the disadvantage that differences in terms of droplet dynamics accumulate over time. Moreover, the instant of contact $\tau = 0$ initiating the coalescence process cannot be unambiguously determined; so, a perfectly synchronous time axis cannot be guaranteed. Therefore, it is advantageous to compare states with equal bridge radius r_b, as shown in Fig. 4.

The superimposed interface contours coincide almost perfectly for all droplet sizes and states, ranging from $r_b/R \approx 0.3$ to 1.3. This indicates that the phase-field model can reproduce the physical behavior very well, since several conditions have to be satisfied for an accurate evolution of the contour. First, the appropriate growth rate of the bridge is crucial. Its growth, driven by the surface tension, induces a stress in the nearby liquid, which can only be relaxed by setting the initially resting bulk liquid into motion. The bridge generates an inward force that pulls the droplets together. The upper bound of this force is given by the surface tension around the circumference of the bridge at its minimum radius.[22]

To better understand the sequence of cause and effect, Figs. 5 and 6 show the evolution of the density and velocity fields resulting from simulations with droplets of initial radius $R = 25$ nm and $R = 50$ nm (the velocity field was only sampled with CFD simulation). To reveal density variations in the droplets, the color map in Fig. 5 was scaled to a narrow range around the saturated liquid density. Since this
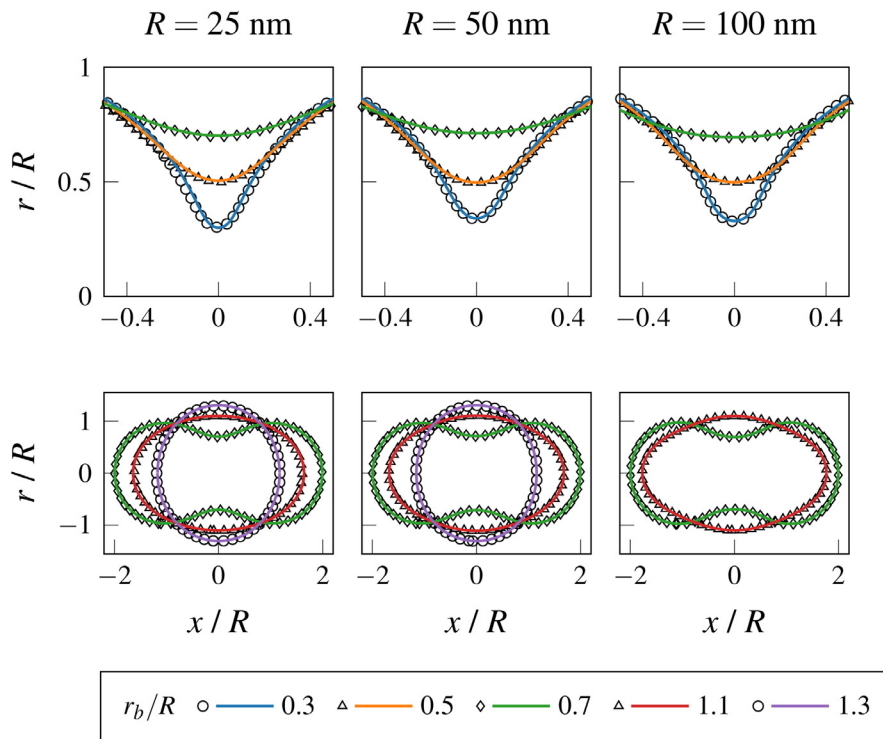

FIG. 4. Comparison of droplet interface contours sampled with MD (symbols) and CFD (solid lines), evaluated at time instances with equal bridge radius r_b. Top: view at the bridge at $r_b/R \approx 0.3$, 0.5, and 0.7. Bottom: global view at $r_b/R \approx 0.7$, 1.1, and 1.3. From left to right, columns show results of simulations with initial droplet radius $R = 25$, 50, and 100 nm. Results for $R = 100$ nm were not sampled until $r_b/R \approx 1.3$ to limit the computational effort.
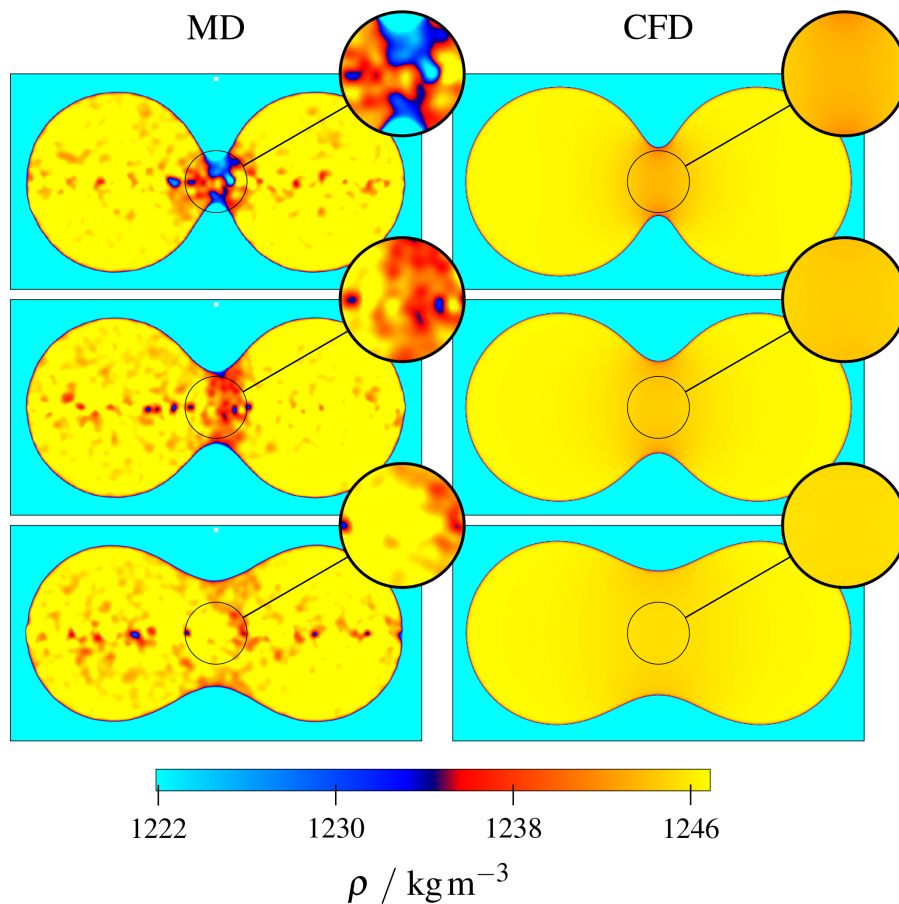
FIG. 5. Density field of droplets with $R = 25$ nm at three instances of time $\tau = 200$ ps (top), 400 ps (center), and 800 ps (bottom) sampled with MD (left) and CFD (right). The color map was scaled to a narrow range around the saturated liquid density. Bridge regions are highlighted by magnified views.

scaling also emphasizes the density fluctuations of the present MD data, ten independent MD simulation runs were averaged for this representation. Both MD and CFD show that early on, the density of the bridge and its vicinity is significantly below the saturation value. This means that the initially rapidly growing bridge releases so much interfacial energy within a very short time that the adjacent fluid layers are subjected to strong tensile forces that generate metastable states with a negative pressure. These volume sections have the ambition to attain physically stable states and hence demand for a supply of molecules from the interior of the droplets to gain density. As a result, fluid layers further away from the bridge accelerate, cf. Fig. 6 (Multimedia view).

From the phase-field model point of view, the sequence of cause and effect can be traced by means of the stress tensor. At the beginning, when the droplets rest, terms of Eq. (4) directly depending on the density gradient or higher derivatives of density dominate the behavior due to the strong curvature of the interface, where the droplets are in contact. This situation gradually transforms to one where the full static pressure contribution determines the evolution of the system. The PeTS EoS is designed such that the Helmholtz energy can also be safely evaluated in the metastable region, yielding the correct negative pressure under such conditions. The pressure gradient is relieved as adjacent liquid layers start to move, generating viscous stress in the neighboring liquid layers at rest, and is finally relaxed by

the global motion of the droplets. The viscous part of the stress tensor determines how fast the local motion can propagate to finally lead to the mutual approach of the droplets. Therein, the shear viscosity describes the resistance to deformation of a fluid element. At low viscosity, as in the present case with $\eta \approx 0.144$ m Pa s, the droplets deform strongly before they start moving, which is opposed by inertial forces. Consequently, the regions further away from the bridge remain at their initial position for a certain period of time, as can be seen from the "back of drop" positions x_{bd}. Therefore, the droplets must constrict to meet the stress from the bridge region, cf. Fig. 7.

The velocity fields in Fig. 6 show that the global motion of the droplets, including their back of drop positions x_{bd}, is not initiated before the bridge has grown to approximately the initial radius R. These observations are consistent with the experiments of Paulsen et al.[22] with varying silicon oils. Droplets with a high viscosity almost rigidly approached each other, whereas the fluid motion was initially limited to the vicinity of the growing bridge in the case of low viscosity.

A quantitative comparison of the MD and CFD simulation results over the entire coalescence process is shown in Fig. 8 by plotting the bridge radius r_b over time after contact τ. A closer look at the very early stages ($\tau < 100$ ps) reveals that the ILV regime, in which the bridge grows with the rate $v_b \sim \gamma/\eta$, is preceded by another
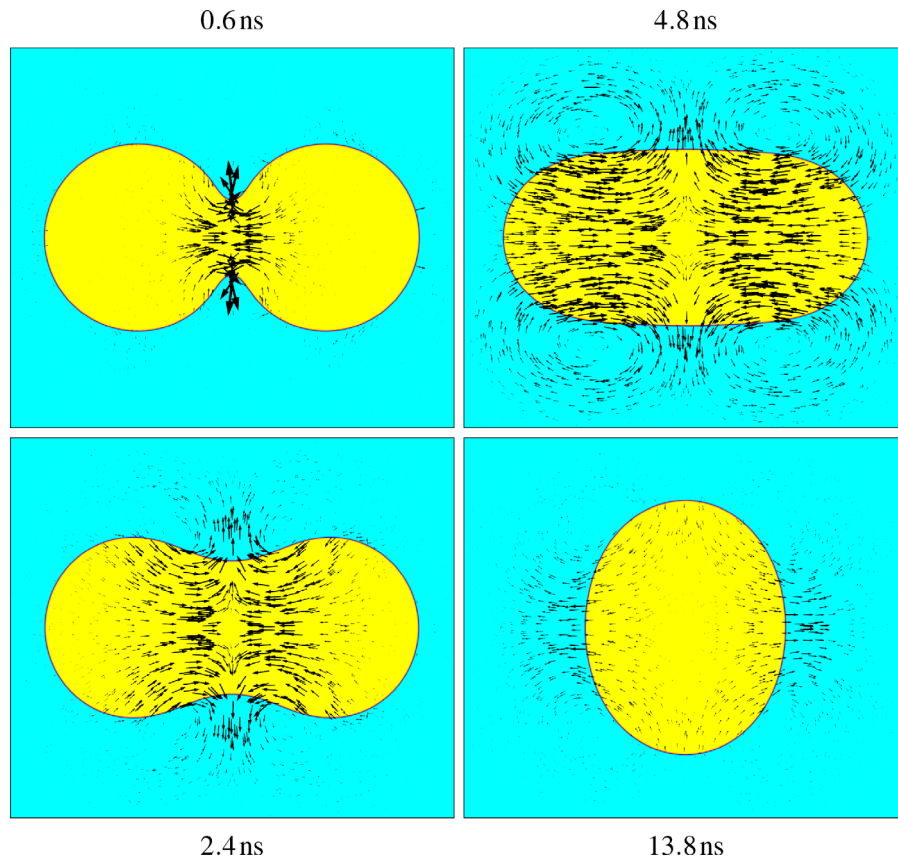
0.6 ns   4.8 ns

FIG. 6. Density and velocity fields of coalescing droplets with an initial radius $R = 50$ nm at four instances of time $\tau = 0.6$, 2.4, 4.8, and 13.8 ns sampled with CFD. Multimedia view: https://doi.org/10.1063/5.0086131.2

2.4 ns   13.8 ns

regime that exhibits a substantially higher growth rate. That thermal regime was identified by Perumanath et al.[39] who investigated coalescing water droplets with MD simulation. They proposed an order of magnitude estimate for the thermal length $l_T \sim l_c$, where l_c is the width of the distribution function describing the probability of

occurrence of the site where the first molecular bridge between the droplets emerges, given by

$$l_c \approx \left(\frac{k_B T}{\gamma}\right)^{1/4} R^{1/2}, \tag{24}$$

with the Boltzmann constant k_B. The probability of occurrence is represented by a normal distribution around the droplet's line of approach where the maximum probability meets the point of smallest distance between the droplets at $r = 0$. This estimate agrees well with the length l_T that we determined at the point where the growth rate transitions to viscous scaling, cf. Fig. 8. For the present argon droplets, however, we found $l_T \approx l_c$ instead of $l_T \approx 2l_c$ as Perumanath et al.[39] did for water droplets. Interestingly, a higher growth rate was also identified in the present CFD simulation results.

From the assumption $l_T \sim l_c$ and Eq. (24), it follows that $l_T/R \sim 1/\sqrt{R}$; so, the thermal regime becomes negligible for macroscopic droplets. In the case of the present nanoscopic droplets, however, the thermal regime plays a dominant role in the early stages of the coalescence process.

Hence, comparing the data shown in Fig. 6 with the asymptotic behavior predicted by theory derived from investigations of macroscopic droplets, where the thermal regime is not considered, may lead to confusion at first sight. For the present droplets, characterized by Oh $\sim 10^{-1}$, cf. Table III, the coalescence phase diagram proposed by
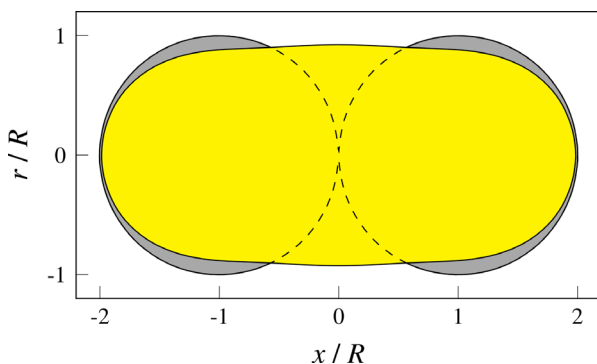

FIG. 7. Superimposed contours of droplets with $R = 100$ nm in their initial state (gray) and coalescing droplets with $r_b/R \approx 1$ (yellow) sampled with MD. At the later stage, global motion of the coalescing droplets just initiated such that the back of drop positions x_{bd} at $x/R \approx \pm 2$ started to move toward the center at $x/R = 0$.
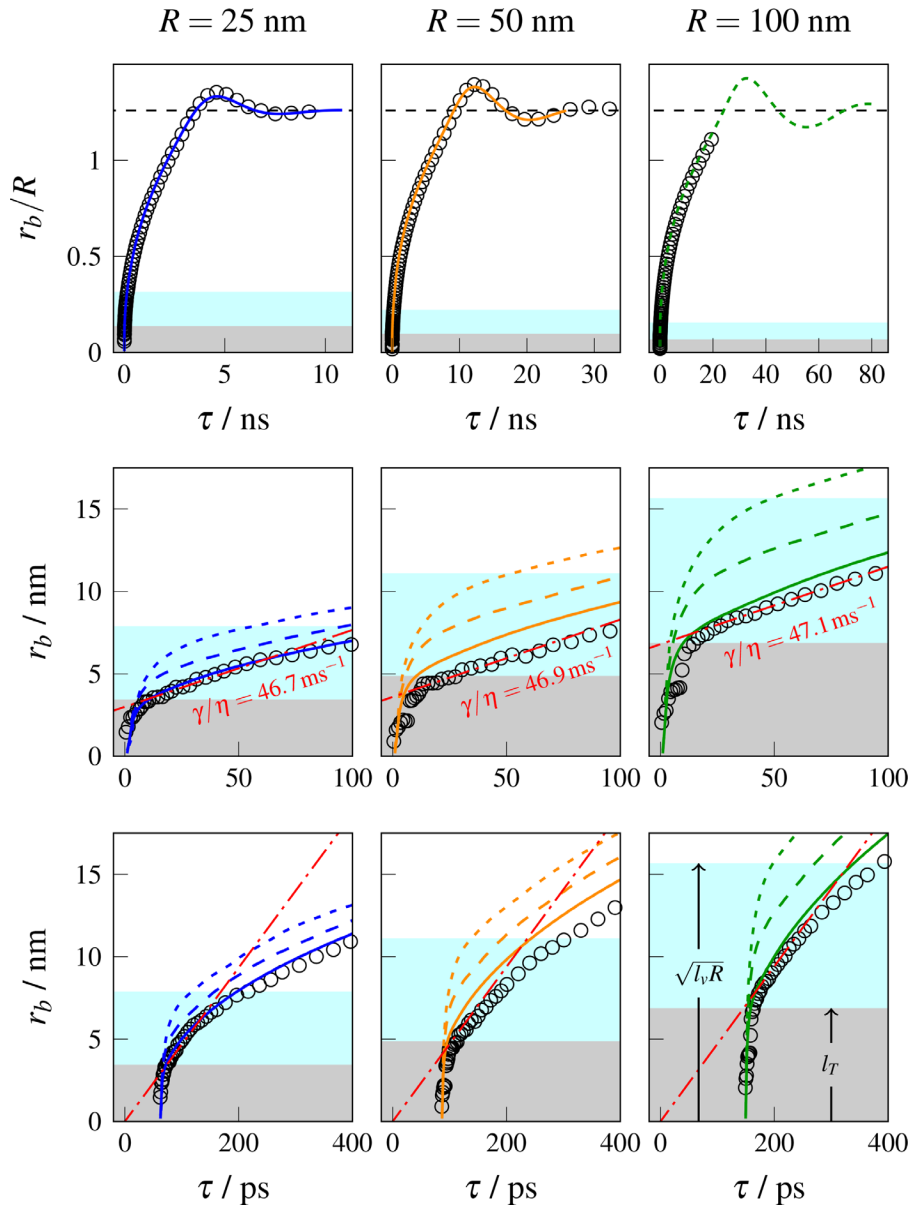
FIG. 8. Temporal evolution of the bridge radius r_b sampled with MD (symbols) and CFD (lines). The statistical uncertainties of the MD data are typically 2% and thereby within symbol size. From left to right, columns show results of simulations with an initial droplet radius $R = 25$, 50, and 100 nm. Shaded areas depict the thermal regime l_T (gray) and the ILV regime $\sqrt{l_v R}$ (blue). Top: global view. CFD results shown for $R = 100$ nm were obtained from a simulation employing the interface widening approach with $\xi = 4$ (short dash), whereas that of $R = 25$ and 50 nm were obtained from simulations without a widened interface (solid). Horizontal lines (dashed) mark the equilibrium state of the merged droplets. Center: view at the early stages. CFD results with and without widened interface are shown, corresponding to $\xi = 1$ (solid), $\xi = 2$ (dashed), and $\xi = 4$ (short dash). The dashed dotted line depicts the growth rate $v_b \sim \gamma/\eta$ of the bridge in the ILV regime, calculated from the surface tension γ and shear viscosity η given in Table III. Bottom: data shifted such that viscous scaling γ/η meets the origin.

Paulsen *et al.*[22] predicts a crossover from the ILV to the inertial regime when the reduced bridge radius attains $r_b/R \sim 10^{-1}$. Based on the condition Re ≈ 1, it can be estimated to occur when the bridge height reaches the viscous length $r_b^2/R \sim l_v$ with

$$l_v = \frac{\eta^2}{\rho\gamma}, \tag{25}$$

which is equivalent to $r_b \sim \sqrt{l_v R}$. Comparing l_T to $\sqrt{l_v R}$ in Table III and Fig. 8 indicates that the thermal regime overrides almost half of the ILV regime. This does not change the bridge radius where the inertial regime is entered, but significantly shortens the time to reach this stage. Hence, before collapsing the present data by rescaling the bridge radius and time axis with respect to the crossover radius $r_b \rightarrow r_b/r_c$

and crossover time $\tau \rightarrow \tau/\tau_c$ as proposed in Ref. 19, we shifted the data by a certain amount of time. Thereby, it was pretended that the thermal regime does not exist and the growth rate corresponds to that of the viscous scaling right from the beginning, cf. Fig. 8 (bottom). The collapse of the shifted data are shown in Fig. 9, exhibiting a rather sharp crossover from the ILV to the inertial regime instead of a smooth transition represented by the interpolation

$$r/r_c = 2\left(\frac{1}{\tau/\tau_c} + \frac{1}{\sqrt{\tau/\tau_c}}\right)^{-1}, \tag{26}$$

proposed in Ref. 19, which we assign to the nanoscopic size of the present droplets.

TABLE III. Parameters characterizing the coalescing droplets, i.e., initial radius R, saturated liquid and vapor densities ρ' and ρ'', shear viscosity η, Ohnesorge number Oh, thermal length l_T, and an estimate for the bridge radius $\sqrt{l_v R}$ where the transition from ILV to inertial regime is expected.

R (nm)	ρ' (kg m^{-3})	ρ'' (kg m^{-3})	η (mPa s)	Oh (–)	l_T (nm)	$\sqrt{l_v R}$ (nm)
25	1247.2	34.16	0.1451	0.3158	3.44	7.89
50	1245.6	33.56	0.1442	0.2222	4.87	11.11
100	1244.8	33.26	0.1438	0.1567	6.88	15.67

Finally, the growth rate of the bridge $v_b = dr_b/d\tau$ and the velocity of the back of drop positions $v_{bd} = dx_{bd}/d\tau$ evaluated from MD and CFD simulation data were directly compared. Therefore, splines were fitted to the temporal evolution of the bridge radius r_b and the back of drop positions' translation $\Delta x_{bd} = 2R - |x_{bd}|$ to obtain smooth velocity profiles, cf. Fig. 10. For a better comparability of the results for the three droplet sizes, units of length and time were reduced by the initial radius R and the inertial time scale τ_i. This illustration emphasizes the agreement between the results of the two simulation methods. Moreover, the similar dynamic behavior of all three droplet sizes points to the applicability of the scaling laws. Evolved in the thermal regime, the initially high bridge growth rate v_b reduces immediately to lower rates after passing the ILV and entering the inertial regime at $\tau_i \approx 1$, were the back of drop positions start moving ($v_{bd} > 0$). Once the maximum back of drop velocity v_{bd} has passed, the bridge radius r_b and the back of drop translation Δx_{bd} reach their maximum at the same time and subsequently the merged droplet starts to oscillate around its equilibrium state, i.e., a resting droplet with a radius of $\approx 2^{1/3}R$. The amplitude and period of this weakly damped oscillation increase for larger droplets due to higher inertial forces.

Because of the rapid dynamics at the beginning, but also for a generally better assignment of the states, a plot over the reduced bridge radius is advantageous, cf. Fig. 11. It reveals that the deviations between the MD and CFD data are mainly limited to the growth rate v_b at the early stages. This can be most clearly seen from the results of $R = 100$ nm, which were obtained from a simulation with a widened interface ($\xi = 4$), showing significant deviations for v_b up to $r_b/R \approx 0.4$. As can be concluded from Fig. 8, this is related to the fact that with a more widened interface, the decrease in the high initial growth rate caused by the strong curvature of the bridge and its meniscus becomes increasingly delayed. This effect seems to be related to the different expression of the contact zone, which expands increasingly in the radial direction with a more widened interface, cf. Fig. 3 (top). On the time axis, however, the part that exhibits these deviations accounts for only a short period due to the high velocity v_b and therefore has only a minor impact on the overall process, cf. Fig. 10. Compared to MD, for CFD simulations the maximum bridge radius r_b was reached slightly more than hundred picoseconds earlier for $R = 25$ nm and about two hundred picoseconds earlier for $R = 50$ nm, corresponding to a relative deviation of about 2%.

Moreover, Fig. 11 shows that the back of drop positions of the largest system start moving when the bridge radius reached the initial radius $r_b/R = 1$, whereas they do so increasingly earlier with smaller droplet size. The oscillation of the velocities v_b and v_{bd} after unification of the droplets manifests itself in this diagram as a spiral, leading to the equilibrium point. The increasing size of the spiral with rising droplet size, best seen for the velocity v_{bd}, again indicates the increasingly strong expression of inertia-induced oscillation.

V. CONCLUSION

Coalescing argon droplets with a radius of 25, 50, and 100 nm were studied with computational methods. Relatively large MD simulations were carried out, containing up to 2×10^8 molecules, to generate reference data. Moreover, a phase-field model resting on a Helmholtz energy EoS was devised that was at the core of CFD simulations. Exactly the same scenarios in terms of geometry, fluid, and state were considered with these approaches. MD and CFD simulation results showed an excellent agreement over the entire coalescence process. Theoretical results on the asymptotic behavior of coalescence process regimes were confirmed. All considered scenarios crossed from the inertially limited viscous regime over to the inertial regime
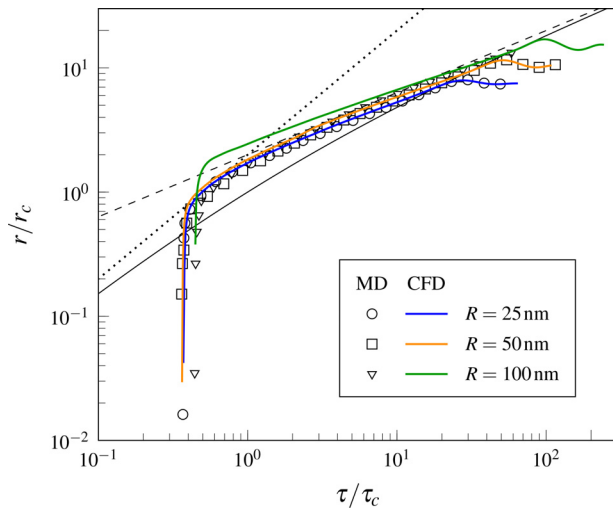

FIG. 9. Bridge radius r_b over time after contact τ sampled with MD (symbols) and CFD (lines). The statistical uncertainties of the MD data are typically 2% and thereby within symbol size. CFD results for $R = 100$ nm were obtained from a simulation employing the interface widening approach with $\xi = 4$, whereas those for $R = 25$ and 50 nm were obtained from simulations without interface widening. The data were shifted, cf. Fig. 8 and related text, and then collapsed by rescaling the horizontal and vertical axes by the crossover time τ_c and the crossover radius r_c of each data set. The limiting behavior is proportional to τ/τ_c (dotted line) at early times and $(\tau/\tau_c)^{1/2}$ at late times (dashed line).[19] A transition between these limiting behaviors is described by Eq. (26) (solid black line).
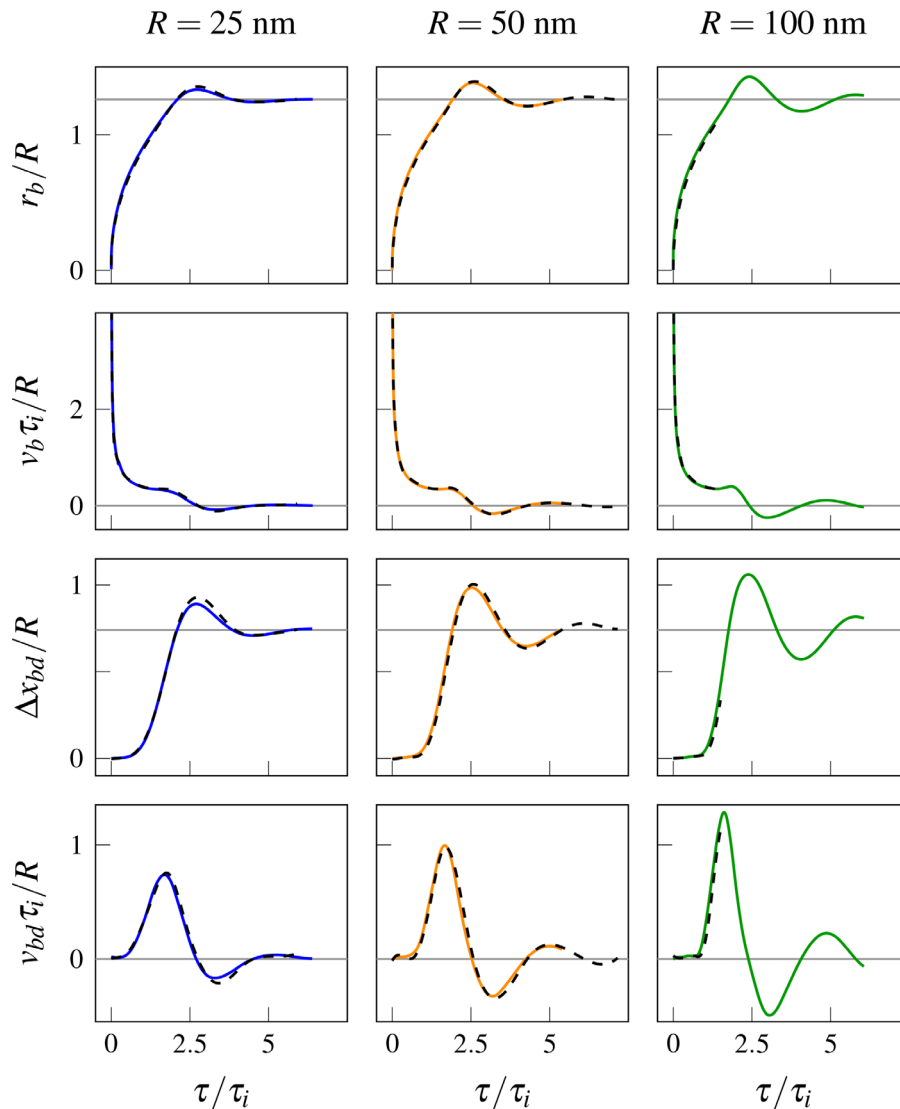
FIG. 10. Temporal evolution of the bridge radius r_b, its growth rate v_b, back of drop positions' translation Δx_{bd}, and its velocity v_{bd}. Profiles of r_b and Δx_{bd} were obtained by fitting splines to the simulation data from MD (dashed line) and CFD (solid line). Profiles of v_b and v_{bd} were then extracted from the first derivatives. CFD results for $R = 100$ nm were obtained from a simulation employing the interface widening approach with $\xi = 4$, whereas those for $R = 25$ and 50 nm were obtained from simulations without interface widening. From left to right, columns show results for an initial droplet radius $R = 25$, 50, and 100 nm. Horizontal lines mark the equilibrium state of the coalesced droplet.

because of the low shear viscosity of argon. The present phase-field model captured the dynamics even at the initial stages of the coalescence process during the thermal regime that was only recently identified by MD simulation. Moreover, a closer look at the liquid density revealed that metastable states associated with negative pressure were attained in the emerging liquid bridge between the coalescing droplets. Thereby, it was demonstrated that the phase-field model is even capable of adequately handling the onset of coalescence.

The vapor–liquid interface, where the surface tension acts, is the crucial element for droplet coalescence and resides on the nanoscale in general. Consequently, a nanoscopic discretization had to be specified for the present CFD simulations resting on the phase-field model. With an interface widening approach, the phase-field model was transferred to coarser grids, while retaining the thermodynamic properties including the surface tension. This allowed for a reduction of the number of grid cells by a factor of 4 ($\xi = 2$) or even 16 ($\xi = 4$), leading to almost the same simulation results with a considerably reduced computational effort. Only in the case of extreme curvatures, as they occur in the early stages of coalescence, increasing deviations from the MD reference data were observed with rising interface widening. However, since strong curvatures are short-lived, they have a minor effect on overall coalescence process.

Another advantage of the phase-field model is its transferability to other fluids, including mixtures. The only requirements are an appropriate Helmholtz energy EoS and expressions for the shear viscosity and surface tension, where for the latter practically only a single state point is needed to adjust the influence parameter. For future work, it seems worthwhile to combine the present phase-field model
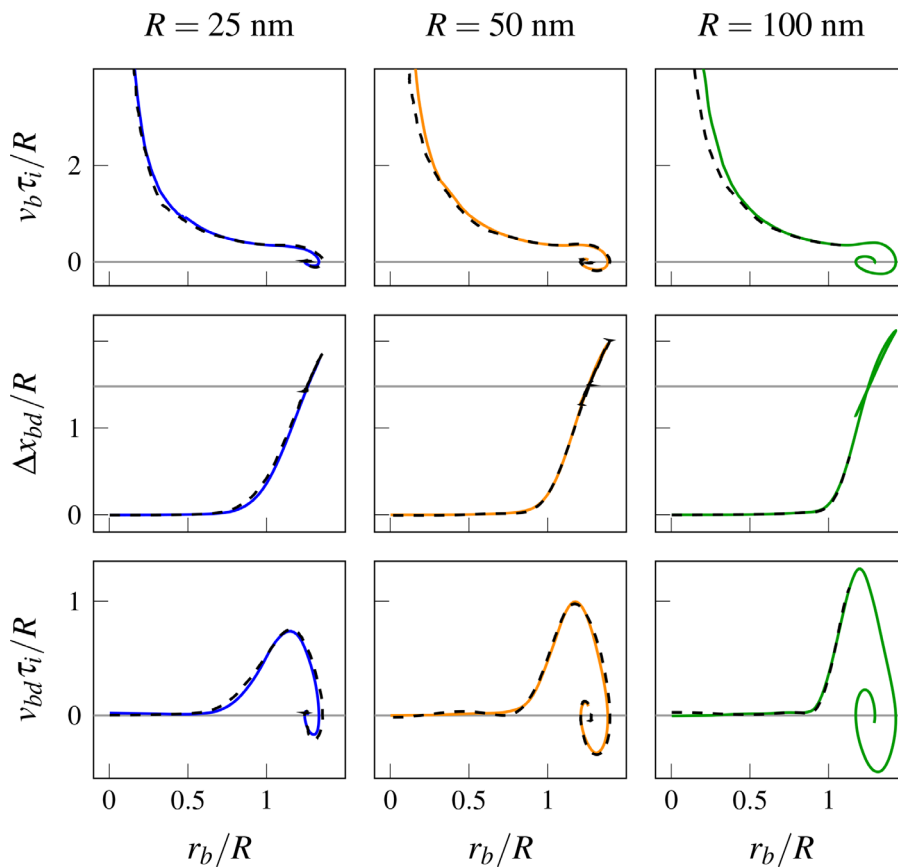
FIG. 11. Growth rate v_b, back of drop positions' translation Δx_{bd} and its velocity v_{bd} plotted over the bridge radius r_b. Profiles of r_b (not shown) and Δx_{bd} were obtained by fitting splines to the simulation data from MD (dashed line) and CFD (solid line). Profiles of v_b and v_{bd} were then extracted from the first derivatives. CFD results for $R = 100$ nm were obtained from a simulation employing the interface widening approach with $\xi = 4$, whereas those for $R = 25$ and 50 nm were obtained from simulations without interface widening. From left to right, columns show results for an initial droplet radius $R = 25$, 50, and 100 nm. Horizontal lines mark the equilibrium state of the coalesced droplet.

with an adaptive grid to further reduce the computational effort and to address macroscopic droplets.

AUTHOR DECLARATIONS
Conflict of Interest

The authors have no conflicts to disclose.

DATA AVAILABILITY

The data that support the findings of this study are openly available in the Data Repository of the University of Stuttgart (DaRUS) at https://doi.org/10.18419/darus-2434, Ref. 66 and https://doi.org/10.18419/darus-2456, Ref. 67.

REFERENCES

[1]F. B. Wadsworth, J. Vasseur, E. W. Llewellin, J. Schauroth, K. J. Dobson, B. Scheu, and D. B. Dingwell, "Sintering of viscous droplets under surface tension," Proc. R. Soc. A **472**, 20150780 (2016).

[2]J. Breitenbach, I. V. Roisman, and C. Tropea, "From drop impact physics to spray cooling models: A critical review," Exp. Fluids **59**, 55 (2018).

[3]J. Jin, C. Ooi, D. Dao, and N.-T. Nguyen, "Coalescence processes of droplets and liquid marbles," Micromachines **8**, 336 (2017).

[4]R. W. Hopper, "Plane Stokes flow driven by capillarity on a free surface," J. Fluid Mech. **213**, 349–375 (1990).

[5]J. Eggers, J. R. Lister, and H. A. Stone, "Coalescence of liquid drops," J. Fluid Mech. **401**, 293–310 (1999).

[6]Y. D. Shikhmurzaev, "Coalescence and capillary breakup of liquid volumes," Phys. Fluids **12**, 2386–2396 (2000).

[7]A. B. Thompson and J. Billingham, "Inviscid coalescence in the presence of a surrounding fluid," IMA J. Appl. Math. **77**, 678–696 (2012).

[8]H. J. Maris, "Analysis of the early stage of coalescence of helium drops," Phys. Rev. E **67**, 066309 (2003).

[9]L. Duchemin, J. Eggers, and C. Josserand, "Inviscid coalescence of drops," J. Fluid Mech. **487**, 167–178 (2003).

[10]T. G. Owe Berg, G. C. Fernish, and T. A. Gaukler, "The mechanism of coalescence of liquid drops," J. Atmos. Sci. **20**, 153–158 (1963).

[11]T. M. Dreher, J. Glass, A. J. O'Connor, and G. W. Stevens, "Effect of rheology on coalescence rates and emulsion stability," AIChE J. **45**, 1182–1190 (1999).

[12]R. Ishiguro, F. Graner, E. Rolley, and S. Balibar, "Coalescence of crystalline drops," Phys. Rev. Lett. **93**, 235301 (2004).

[13]M. Wu, T. Cubaud, and C.-M. Ho, "Scaling law in liquid drop coalescence driven by surface tension," Phys. Fluids **16**, L51–L54 (2004).

[14]D. G. A. L. Aarts, H. N. W. Lekkerkerker, H. Guo, G. H. Wegdam, and D. Bonn, "Hydrodynamics of droplet coalescence," Phys. Rev. Lett. **95**, 164503 (2005).

[15]S. T. Thoroddsen, K. Takehara, and T. G. Etoh, "The coalescence speed of a pendent and a sessile drop," J. Fluid Mech. **527**, 85–114 (2005).

[16]K. Fezzaa and Y. Wang, "Ultrafast x-ray phase-contrast imaging of the initial coalescence phase of two water droplets," Phys. Rev. Lett. **100**, 104501 (2008).

[17]S. C. Case, "Coalescence of low-viscosity fluids in air," Phys. Rev. E **79**, 026307 (2009).

[18]S. T. Thoroddsen, B. Qian, T. G. Etoh, and K. Takehara, "The initial coalescence of miscible drops," Phys. Fluids **19**, 072110 (2007).

[19]J. D. Paulsen, J. C. Burton, and S. R. Nagel, "Viscous to inertial crossover in liquid drop coalescence," Phys. Rev. Lett. **106**, 114501 (2011).

[20]M. M. Rahman, W. Lee, A. Iyer, and S. J. Williams, "Viscous resistance in drop coalescence," Phys. Fluids **31**, 012104 (2019).

[21]A. Menchaca-Rocha, A. Martínez-Dávalos, R. Núñez, S. Popinet, and S. Zaleski, "Coalescence of liquid drops by surface tension," Phys. Rev. E **63**, 046309 (2001).

[22]J. D. Paulsen, J. C. Burton, S. R. Nagel, S. Appathurai, M. T. Harris, and O. A. Basaran, "The inexorable resistance of inertia determines the initial regime of drop coalescence," Proc. Natl. Acad. Sci. U. S. A. **109**, 6857–6861 (2012).

[23]J. D. Paulsen, "Approach and coalescence of liquid drops in air," Phys. Rev. E **88**, 063010 (2013).

[24]Y. Chen, C. Shen, and G. P. Peterson, "Hydrodynamics and morphologies of droplet coalescence," Ind. Eng. Chem. Res. **54**, 9257–9262 (2015).

[25]C. Shen, Y. Chen, C. Yu, and X. Liu, "Numerical study on the liquid-liquid interface evolution during droplet coalescence," Microgravity Sci. Technol. **32**, 737–748 (2020).

[26]P. Zimmermann, A. Mawbey, and T. Zeiner, "Calculation of droplet coalescence in binary liquid–liquid systems: An incompressible Cahn–Hilliard/Navier–Stokes approach using the non-random two-liquid model," J. Chem. Eng. Data **65**, 1083–1094 (2020).

[27]L. Baroudi, M. Kawaji, and T. Lee, "Effects of initial conditions on the simulation of inertial coalescence of two drops," Comput. Math. Appl. **67**, 282–289 (2014).

[28]S. J. Lim, M. C. Choi, B. M. Weon, and B. Gim, "Lattice Boltzmann simulations for water coalescence," Appl. Phys. Lett. **111**, 101602 (2017).

[29]M. Gross, I. Steinbach, D. Raabe, and F. Varnik, "Viscous coalescence of droplets: A lattice Boltzmann study," Phys. Fluids **25**, 052101 (2013).

[30]J. E. Sprittles and Y. D. Shikhmurzaev, "Coalescence of liquid drops: Different models versus experiment," Phys. Fluids **24**, 122105 (2012).

[31]R. T. Eiswirth, H.-J. Bart, A. A. Ganguli, and E. Y. Kenig, "Experimental and numerical investigation of binary coalescence: Liquid bridge building and internal flow fields," Phys. Fluids **24**, 062108 (2012).

[32]J.-C. Pothier and L. J. Lewis, "Molecular-dynamics study of the viscous to inertial crossover in nanodroplet coalescence," Phys. Rev. B **85**, 115447 (2012).

[33]H. Deka, G. Biswas, S. Chakraborty, and A. Dalal, "Coalescence dynamics of unequal sized drops," Phys. Fluids **31**, 012105 (2019).

[34]R. Stierle and J. Gross, "Hydrodynamic density functional theory for mixtures from a variational principle and its application to droplet coalescence," J. Chem. Phys. **155**, 134101 (2021).

[35]A. H. Rajkotwala, H. Mirsandi, E. A. J. F. Peters, M. W. Baltussen, C. W. M. van der Geld, J. G. M. Kuerten, and J. A. M. Kuipers, "Extension of local front reconstruction method with controlled coalescence model," Phys. Fluids **30**, 022102 (2018).

[36]J.-Y. Chen, P. Gao, Y.-T. Xia, E.-Q. Li, H.-R. Liu, and H. Ding, "Early stage of delayed coalescence of soluble paired droplets: A numerical study," Phys. Fluids **33**, 092005 (2021).

[37]V. Cristini and Y.-C. Tan, "Theory and numerical simulation of droplet dynamics in complex flows—A review," Lab Chip **4**, 257–264 (2004).

[38]J. Kamp, J. Villwock, and M. Kraume, "Drop coalescence in technical liquid/liquid applications: A review on experimental techniques and modeling approaches," Rev. Chem. Eng. **33**, 1–47 (2017).

[39]S. Perumanath, M. K. Borg, M. V. Chubynsky, J. E. Sprittles, and J. M. Reese, "Droplet coalescence is initiated by thermal motion," Phys. Rev. Lett. **122**, 104501 (2019).

[40]J. Koplik, S. Pal, and J. R. Banavar, "Dynamics of nanoscale droplets," Phys. Rev. E **65**, 021504 (2002).

[41]L. Zhao and P. Choi, "Molecular dynamics simulation of the coalescence of nanometer-sized water droplets in n-heptane," J. Chem. Phys. **120**, 1935–1942 (2004).

[42]B.-B. Wang, X.-D. Wang, W.-M. Yan, and T.-H. Wang, "Molecular dynamics simulations on coalescence and non-coalescence of conducting droplets," Langmuir **31**, 7457–7462 (2015).

[43]T. Li, Y. Xia, L. Zhang, X. Zhang, C. Fu, Y. Jiang, and H. Li, "Effects of stripy surfaces with intervals on the coalescence dynamics of nano-droplets: Insights from molecular dynamics simulations," Appl. Surf. Sci. **481**, 951–959 (2019).

[44]S. Grottel, M. Krone, C. Muller, G. Reina, and T. Ertl, "MegaMol—A prototyping framework for particle-based visualization," IEEE Trans. Visualization Comput. Graph. **21**, 201–214 (2015).

[45]P. J. Hoogerbrugge and J. M. V. A. Koelman, "Simulating microscopic hydrodynamic phenomena with dissipative particle dynamics," Europhys. Lett. **19**, 155–160 (1992).

[46]V. Akella and H. Gidituri, "Universal scaling laws in droplet coalescence: A dissipative particle dynamics study," Chem. Phys. Lett. **758**, 137917 (2020).

[47]N. Moelans, B. Blanpain, and P. Wollants, "An introduction to phase-field modeling of microstructure evolution," CALPHAD **32**, 268–294 (2008).

[48]D. M. Anderson, G. B. McFadden, and A. A. Wheeler, "Diffuse-interface methods in fluid mechanics," Annu. Rev. Fluid Mech. **30**, 139–165 (1998).

[49]V. E. Badalassi, H. D. Ceniceros, and S. Banerjee, "Computation of multiphase systems with phase field models," J. Comput. Phys. **190**, 371–397 (2003).

[50]D. Jacqmin, "Calculation of two-phase Navier–Stokes flows using phase-field modeling," J. Comput. Phys. **155**, 96–127 (1999).

[51]J. W. Cahn and J. E. Hilliard, "Free energy of a nonuniform system. I. Interfacial free energy," J. Chem. Phys. **28**, 258–267 (1958).

[52]J. Gross and G. Sadowski, "Perturbed-chain SAFT: An equation of state based on a perturbation theory for chain molecules," Ind. Eng. Chem. Res. **40**, 1244–1260 (2001).

[53]M. Heier, S. Stephan, J. Liu, W. G. Chapman, H. Hasse, and K. Langenbach, "Equation of state for the Lennard-Jones truncated and shifted fluid with a cut-off radius of 2.5σ based on perturbation theory and its applications to interfacial thermodynamics," Mol. Phys. **116**, 2083–2094 (2018).

[54]K. Langenbach, "Co-oriented fluid functional equation for electrostatic interactions (COFFEE)," Chem. Eng. Sci. **174**, 40–55 (2017).

[55]H. Kahl and S. Enders, "Calculation of surface properties of pure fluids using density gradient theory and SAFT-EOS," Fluid Phase Equilib. **172**, 27–42 (2000).

[56]C. Miqueu, B. Mendiboure, A. Graciaa, and J. Lachaise, "Modelling of the surface tension of pure components with the gradient theory of fluid interfaces: A simple and accurate expression for the influence parameters," Fluid Phase Equilib. **207**, 225–246 (2003).

[57]P. Rehner and J. Gross, "Predictive density gradient theory based on nonlocal density functional theory," Phys. Rev. E **98**, 063312 (2018).

[58]F. Diewald, M. Heier, M. Horsch, C. Kuhn, K. Langenbach, H. Hasse, and R. Müller, "Three-dimensional phase field modeling of inhomogeneous gas-liquid systems using the PeTS equation of state," J. Chem. Phys. **149**, 064701 (2018).

[59]S. Stephan, K. Langenbach, and H. Hasse, "Interfacial properties of binary lennard-jones mixtures by molecular simulation and density gradient theory," J. Chem. Phys. **150**, 174704 (2019).

[60]F. Diewald, M. P. Lautenschlaeger, S. Stephan, K. Langenbach, C. Kuhn, S. Seckler, H.-J. Bungartz, H. Hasse, and R. Müller, "Molecular dynamics and phase field simulations of droplets on surfaces with wettability gradient," Comput. Methods Appl. Mech. Eng. **361**, 112773 (2020).

[61]M. P. Lautenschlaeger and H. Hasse, "Transport properties of the Lennard-Jones truncated and shifted fluid from non-equilibrium molecular dynamics simulations," Fluid Phase Equilib. **482**, 38–47 (2019).

[62]J. Vrabec, G. K. Kedia, G. Fuchs, and H. Hasse, "Comprehensive study of the vapour–liquid coexistence of the truncated and shifted Lennard–Jones fluid including planar and spherical interface properties," Mol. Phys. **104**, 1509–1527 (2006).

[63]C. Niethammer, S. Becker, M. Bernreuther, M. Buchholz, W. Eckhardt, A. Heinecke, S. Werth, H.-J. Bungartz, C. W. Glass, H. Hasse, J. Vrabec, and M. Horsch, "ls1 mardyn: The massively parallel molecular dynamics code for large systems," J. Chem. Theory Comput. **10**, 4455–4464 (2014).

[64]N. Tchipev, S. Seckler, M. Heinen, J. Vrabec, F. Gratl, M. Horsch, M. Bernreuther, C. W. Glass, C. Niethammer, N. Hammer, B. Krischok, M. Resch, D. Kranzlmüller, H. Hasse, H.-J. Bungartz, and P. Neumann, "TweTriS: Twenty trillion-atom simulation," Int. J. High Perform. Comput. Appl. **33**, 838–854 (2019).

[65]F. Diewald, "Phase field modeling of static and dynamic wetting," *Forschungsbericht/Technische Universität Kaiserslautern* (Lehrstuhl Technische Mechanik, 2020), Vol. 19.

[66]M. Heinen and J. Vrabec, *Coalescence of Two Nanoscopic Argon Droplets by Molecular Dynamics Simulation* (University of Stuttgart, 2022).

[67]M. Hoffmann, F. Diewald, and K Langenbach, *Coalescence of Two Nanoscopic Argon Droplets by Phase-Field Modeling* (University of Stuttgart, 2022).